THE JOURNAL OF BIOLOGICAL CHEMISTRY VOL. 289, NO. 50, pp. 34530–34542, December 12, 2014
Published in the U.S.A.

Calsyntenin-3 Molecular Architecture and Interaction with Neurexin 1α*[S]

Received for publication, September 2, 2014, and in revised form, October 25, 2014 Published, JBC Papers in Press, October 28, 2014, DOI 10.1074/jbc.M114.606806

Zhuoyang Lu[‡§1], Yun Wang[¶1], Fang Chen[¶], Huimin Tong[‡], M. V. V. V. Sekhar Reddy[‖], Lin Luo[**], Suchithra Seshadrinathan[‖], Lei Zhang[‡], Luis Marcelo F. Holthauzen[‡‡], Ann Marie Craig[**], Gang Ren[‡2], and Gabby Rudenko[‖‡‡3]

From the [‖]Department of Pharmacology and Toxicology and the [‡‡]Sealy Center for Structural Biology and Molecular Biophysics, University of Texas Medical Branch, Galveston Texas 77555, the [‡]Molecular Foundry, Lawrence Berkeley National Laboratory, Berkeley, California 94720, the [§]School of Life Science and Technology and Frontier Institute of Science and Technology, Xi'an Jiaotong University, Xi'an 710049, China, the [**]Department of Psychiatry, University of British Columbia, Vancouver V6T 2A1, Canada, and the [¶]University of Michigan, Ann Arbor, Michigan 48109

Background: Calsyntenin-3 (Cstn3) promotes synapse development, controversially interacting with neurexin 1α (n1α).
Results: Cstn3 binds n1α directly, and its structure adopts multiple forms.
Conclusion: Cstn3 interacts with n1α via a novel mechanism and can produce distinct trans-synaptic bridges with n1α.
Significance: A complex portfolio of molecular interactions between proteins implicated in autism spectrum disorder and schizophrenia guide synapse development.

Calsyntenin 3 (Cstn3 or Clstn3), a recently identified synaptic organizer, promotes the development of synapses. Cstn3 localizes to the postsynaptic membrane and triggers presynaptic differentiation. Calsyntenin members play an evolutionarily conserved role in memory and learning. Cstn3 was recently shown in cell-based assays to interact with neurexin 1α (n1α), a synaptic organizer that is implicated in neuropsychiatric disease. Interaction would permit Cstn3 and n1α to form a trans-synaptic complex and promote synaptic differentiation. However, it is contentious whether Cstn3 binds n1α directly. To understand the structure and function of Cstn3, we determined its architecture by electron microscopy and delineated the interaction between Cstn3 and n1α biochemically and biophysically. We show that Cstn3 ectodomains form monomers as well as tetramers that are stabilized by disulfide bonds and Ca^{2+}, and both are probably flexible in solution. We show further that the extracellular domains of Cstn3 and n1α interact directly and that both Cstn3 monomers and tetramers bind n1α with nanomolar affinity. The interaction is promoted by Ca^{2+} and requires minimally the LNS domain of Cstn3. Furthermore, Cstn3 uses a fundamentally different mechanism to bind n1α compared with other neurexin partners, such as the synaptic organizer neuroligin 2, because Cstn3 does not strictly require the sixth LNS domain of n1α. Our structural data suggest how Cstn3 as a synaptic organizer on the postsynaptic membrane, particularly in tetrameric form, may assemble radially symmetric trans-synaptic bridges with the presynaptic synaptic organizer n1α to recruit and spatially organize proteins into networks essential for synaptic function.

A growing number of synaptic organizers form heterophilic trans-synaptic molecular bridges to mediate synaptic differentiation (the assembly and maintenance of presynaptic and postsynaptic machineries capable of synaptic transmission) (1, 2). Many of these synaptic organizers are now implicated in neuropsychiatric disorders, underscoring their importance in regulating functional neuronal circuits (2). Calsyntenin-3 (Cstn3[4] or Clstn3) was recently identified as a synapse-organizing protein (3), and its role was confirmed by multiple groups (4). Cstn3 localizes in part to the postsynaptic membrane (5). On the cell surface, Cstn3 triggers inhibitory and excitatory presynaptic differentiation in contacting axons (3). Cstn3 knock-out mice display both decreased inhibitory and excitatory synaptic densities and deficits in synaptic transmission, suggesting that Cstn3 is needed for the development of both GABAergic and glutamatergic synapses (3). Members of the calsyntenin family play a role in learning and memory (6–8). Calsyntenins have also been linked to Alzheimer disease and appear to shield amyloid-β precursor protein from the proteolytic production of amyloidogenic Aβ peptide (9–11). The extracellular domain of calsyntenins is composed of two cadherin domains, an LNS (laminin, neurexin, sex hormone-binding globulin) domain and an α-helix/β-strand-containing domain (α/β domain). Calsyntenins are proteolytically cleaved (9), and their shed ectodo-

* This work was supported, in whole or in part, by National Institutes of Health, NIMH, Grants R01MH077303 and R01MH070860. This work was also supported by the Sealy Center for Structural Biology and Molecular Biophysics (UTMB) and the Brain and Behavior Research Foundation. Work at the Molecular Foundry was supported by the United States Department of Energy under Contract DE-AC02-05CH11231.
[S] This article contains supplemental Figs. S1 and S2.
[1] Both authors contributed equally to this work.
[2] To whom correspondence may be addressed: Lawrence Berkeley National Laboratory, Molecular Foundry Rm. 2220, 1 Cyclotron Rd., MS 67R2206, Berkeley, CA 94720. Tel.: 510-495-2375; Fax: 510-486-7268; E-mail: gren@lbl.gov.
[3] To whom correspondence may be addressed: Dept. of Pharmacology/Toxicology and the Sealy Center for Structural Biology, University of Texas Medical Branch, 301 University Blvd., Galveston, TX 77555. Tel.: 409-772-6292; E-mail: garudenk@utmb.edu.
[4] The abbreviations used are: Cstn3, calsyntenin 3; n1α, neurexin 1α; LMW, low molecular weight; HMW, high molecular weight; IPET, individual particle electron tomography; FSC, Fourier shell correlation; NL2, neuroligin 2; CFP, cyan fluorescent protein.

main can oppose the function of the full-length calsyntenin (3). The Cstn3 ectodomain was shown to bind the extracellular domain of neurexin 1α (n1α), a synaptic organizer found on the presynaptic membrane, in synaptosomal pull-down assays and cell-based binding and recruitment assays (3) as well as via independent proteomic approaches in our laboratory. However, Um *et al.* (4) were not able to reproduce the interaction between Cstn3 and n1α in similar cell surface binding assays, raising a question of whether Cstn3 binds n1α directly.

Neurexins bind multiple partners, including neuroligins, LRRTMs, and cerebellins, and trigger postsynaptic differentiation in contacting dendrites (*i.e.* the recruitment of a functional postsynaptic machinery) (1, 2). Importantly, neurexins, neuroligins, and LRRTMs are all implicated in a number of neuropsychiatric diseases (12–14). Neurexin genes each encode a longer α and a shorter β form (15). n1α is composed of six LNS domains (L1–L6) interspersed by three EGF-like repeats (A, B, and C) forming an L-shaped core (16, 17). Neurexin mRNA transcripts are diversified through alternative splicing (18). Neurexin LNS domains contain a "hypervariable surface" at one end of their β-sandwich fold formed by loops that host splice inserts and a central Ca^{2+}-binding site (19, 20). Neuroligins bind to the hypervariable surface of the n1β LNS domain (identical to n1α L6), whereas LRRTMs share an overlapping binding site (21–25). Most, but not all, protein partners appear to interact with the hypervariable surfaces of neurexin LNS domains regulated by the presence of splice inserts and/or Ca^{2+}.

To gain insight into the structure and function of Cstn3, we used biochemical, biophysical, and structural methods to interrogate Cstn3 and its interaction with n1α. We show that the extracellular domain of Cstn3 forms both functional monomers and tetramers, and we reveal their architectures and demonstrate direct interaction between Cstn3 and n1α. Our results suggest that Cstn3 works in concert with n1α by forming a trans-synaptic bridge to promote synapse development.

EXPERIMENTAL PROCEDURES

Protein Expression and Purification

The human Csnt3 ectodomain or fragments (accession number BC104767), followed by a C-terminal tag ASTSHHHHHH, was produced using baculovirus-mediated overexpression in HighFive cells with Insect-XPRESS + L-glutamine medium (Lonza). Briefly, medium containing the secreted proteins was concentrated after protease inhibitors were added, dialyzed overnight (25 mM sodium phosphate, pH 8.0, 250 mM NaCl), and purified with a nickel-nitrilotriacetic acid column (Invitrogen; 25 mM sodium phosphate, pH 8, 500 mM NaCl, eluted with an imidazole gradient). Subsequently, the protein was dialyzed into 25 mM Tris, pH 8, 100 mM NaCl, 0.5 mM PMSF; incubated with 5 mM $CaCl_2$ for 0.5 h; applied to a MonoQ column (GE Healthcare) equilibrated with 25 mM Tris, pH 8, 50 mM NaCl; and subsequently eluted with an NaCl gradient. Cstn3-LMW and Cstn3-HMW eluted separately on the MonoQ column. Last, proteins were applied to a HiLoad Superdex-200 16/60 size exclusion column (GE Healthcare; 25 mM Tris, pH 8, 100 mM NaCl). Purified proteins were stored in 25 mM Tris, pH 8, 100 mM NaCl in flash-frozen aliquots. Purified hexahistidine-tagged bovine neurexin 1α and its fragments as well as hexahistidine-tagged rat neuroligin 2 (NL2) containing insert +A2 were produced in a manner similar to that described previously (16). Recombinant rat neurexin 1β was produced as described (26). For analytical size exclusion chromatography, proteins were loaded on a Superdex 200 PC 3.2/30 column in 25 mM Tris, pH 8.0, 120 mM NaCl, 5 mM $CaCl_2$ and run at 0.08 ml/min. Protein standards (Sigma; 200, 66, 29, and 12.4 kDa) and blue dextran (2000 kDa) were used to calibrate the column loaded in a 50-μl sample volume and run at 0.08 ml/min.

Electron Microscopy

Negative Stain EM Specimen Preparation—Cstn3-LMW samples (monomer, calculated molecular mass 88 kDa) and Cstn3-HMW (tetramer, calculated molecular mass 352 kDa) were prepared by negative stain. In brief, the Cstn3-LMW sample (monomer) at ~1.0 mg/ml was diluted to ~0.02 mg/ml in 25 mM Tris, pH 8, 100 mM NaCl, 3 mM $CaCl_2$. The Cstn3-HMW sample (tetramer) at ~1.0 mg/ml was diluted to ~0.05 mg/ml in the same buffer. An aliquot (~4 μl) of sample was placed on a glow-discharged (15 s) thin carbon-coated 200-mesh copper grid (CF200-Cu, EMS). After ~1 min of incubation, excess solution was blotted with filter paper, and the grid was stained for ~1 min by submersion in a drop (~35 μl) of 1% (w/v) uranyl formate (27, 28) before nitrogen air drying at room temperature.

EM Data Acquisition and Image Preprocessing—The negative stain micrographs were acquired at room temperature on a Gatan UltraScan 4K×4K CCD by a Zeiss Libra 120 transmission EM (Carl Zeiss NTS) operating at 120 kV at ×125,000 magnification (0.94 Å/pixel) under low defocus (−0.1 to ~−0.6 μm) by following a strategy developed for imaging small and asymmetric proteins (28). The micrograph defocus and astigmatism were examined by *ctffind3* (FREALIGN software package) (29). Micrographs with distinguishable drift effects were excluded, and the rest were corrected for the contrast transfer function with the SPIDER software (30). Only isolated particles were initially selected and windowed by the EMAN software (31) and then manually adjusted. A total of 11,186 Cstn3-LMW particles and 6699 Cstn3-HMW particles were windowed and selected from 1063 micrographs. These particles were then aligned and classified by reference-free class averaging using *refine2d.py* (EMAN).

Electron Tomography (ET) Data Acquisition and Image Preprocessing—ET data of Cstn3-LMW and Cstn3-HMW were acquired with the equipment and conditions described above. The specimens on a high tilt room temperature holder were tilted at angles ranging from −66 to 66° in steps of 1.5°. The tilt series were acquired under a total electron dose of ~200 $e^-/Å^2$ by the Gatan tomography software. The tilt series were initially aligned together with the IMOD software package (32), and the contrast transfer function was determined by *ctffind3* (FREALIGN software) and corrected by TOMOCTF (33). The tilt series for a singled out ("targeted") Cstn3 particle was tracked and selected at 150 × 150-pixel size.

Individual Particle Electron Tomography (IPET) Three-dimensional Reconstruction—*Ab initio* three-dimensional reconstructions were conducted using the IPET reconstruction method (34). In brief, the tilt series of a targeted particle was directly back-projected into a three-dimensional map to generate an "initial model." The projections of the initial model were then used as the references for tilting image alignment. During this process, a set of automatically generated Gaussian low pass filters and automatically generated masks were sequentially applied to both the references and tilt images. The three-dimensional map from the previous iteration was used as the new initial model for the next iteration until the changes in translational parameters were less than 1 pixel in total.

IPET Fourier Shell Correlation (FSC) Analysis—The resolutions of the IPET three-dimensional reconstructions were determined by FSC analysis by splitting the center refined raw ET images into two groups (odd- or even-numbered indices according to the order of tilting angles). Each group was used independently to generate a three-dimensional reconstruction by IPET; the two IPET three-dimensional reconstructions were then used to compute the FSC curve over their corresponding spatial frequency shells in Fourier space (using the "*RF 3*" command in SPIDER) (30). The frequency at which the FSC curve fell to a value of 0.5 was used to assess the resolution of the final IPET three-dimensional density map.

Single-particle Three-dimensional Reconstruction—Two IPET three-dimensional density maps of Cstn3-LMW (monomer) and two IPET maps of Cstn3-HMW (tetramer) were low pass-filtered to 26 and 30 Å, respectively. The maps were then used as *ab initio* initial models for their corresponding single-particle multireference refinement (*multirefine* in EMAN) (31). The final maps refined from the two Cstn3-LMW (monomer) particles showed a resolution of 15.0 and 15.9 Å, respectively (based on the 0.5 FSC criterion (31)), whereas the final maps refined from the two Cstn3-HMW (tetramer) particles showed a resolution of 16.0 and 16.5 Å, respectively. For the Cstn3-HMW (tetramer) refinement, C_4 symmetry was enforced. All maps were then low pass-filtered to 16 Å for structural manipulation. Domains were roughly assigned and colored using *Color Zone* in Chimera (35) by fitting homology models of the Cad1-Cad2 tandem and the LNS domain, whereas the remaining molecular volume was assigned to the α/β domain. As a basis for Cstn3 Cad1-Cad2, Cad2-Cad3 (also known as EC2-EC3) from mouse cadherin-8 (Protein Data Bank entry 2A62 (36)) was used and has 25.5% sequence identity to the human Cstn3 counterpart. For the Cstn3 LNS domain, the LNS domain L2 from the rat n1α (Protein Data Bank 2H0B (20)) was used and has 23.4% sequence identity to the human Cstn3 counterpart.

To compare the two final Cstn3-HMW tetramer maps, they were aligned by *proc3d* and *align3d* (EMAN) before FSC computation. The subunits within each tetramer density map were extracted using the *Volume Eraser* option and then aligned to the Cstn3 monomer (monomer reconstruction 2) by optimizing the maximal cross-correlation of density maps with a contour level of ~25 kDa using Chimera. The aligned density maps were further aligned prior to FSC calculation. The rotational autocorrelation was computed using the *measure rotation* and *measure corr* commands in Chimera.

Statistical Analyses of the Particle Size—A total of 1776 Cstn3-LMW particles, 1033 Cstn3-HMW particles in the presence of 3 mM $CaCl_2$, and 1017 Cstn3-HMW particles without additional Ca^{2+} were selected from a total of 722 micrographs. Only "top view" Cstn3-HMW particles were used to measure the diameter in two orthogonal directions. The longest dimension of the Cstn3 monomer particle was used to represent its size. The geometric mean (the square root of the product) of two perpendicular diameters was used to represent the diameter of the Cstn3 tetramer. Histograms for the dimensions of the particles were generated and fitted with a Gaussian function in Origin version 7.5 (sampling step of 5.0 Å). Four density maps have been deposited to the Electron Microscopy Data Bank (EMD-6009, EMD-6010, EMD-6011, and EMD-6012).

Solid Phase Binding Assays

Proteins were biotinylated at room temperature by dialyzing them into PBS (100 mM sodium phosphate, pH 7.2, 150 mM NaCl), subsequently incubating them with a 5-fold molar excess of EZ-Link NHS PEG4-Biotin (Pierce) for 30 min and then dialyzing them into 25 mM Tris, pH 8, 100 mM NaCl. The labeling efficiency was typically 4–8 biotins/molecule as determined by the Pierce biotin quantitation kit. Solid phase binding assays were carried out at room temperature. For assays with immobilized neurexins, 200 ngr neurexin in binding buffer/Ca^{2+} (20 mM Tris, pH 8.0, 100 mM NaCl, 5 mM $CaCl_2$) was coated in 96-well plates (Corning Costar 9017) for 2 h at 150 rpm. As a background control, a series of wells was incubated with buffer but no neurexin. The wells were subsequently emptied; washed three times with 300 μl of binding buffer/Ca^{2+} for 30 s at 400 rpm or, for Ca^{2+}-free conditions, with binding buffer/EDTA (20 mM Tris, pH 8.0, 100 mM NaCl, 20 mM EDTA); and finally blocked with blocking buffer (2% (w/v) gelatin (Sigma G7663) in binding buffer/Ca^{2+} or binding buffer/EDTA) for 2 h. Wells were then incubated with increasing concentrations of biotinylated Cstn3-LMW*, Cstn3-HMW*, or NL2* in binding buffer/Ca^{2+} with 0.25% BSA (in triplicate) or binding buffer/EDTA (20 mM Tris, pH 8.0, 100 mM NaCl, 20 mM EDTA) with 0.25% BSA (in duplicate) for 1 h, emptied, and washed again three times with binding buffer/Ca^{2+} or binding buffer/EDTA. For assays with immobilized Cstn3, 200 ngr Cstn3 (or fragments) in binding buffer/Ca^{2+} was coated for 1 h at 150 rpm, and the wells were treated as described above except that they were blocked with blocking buffer containing 3% gelatin. Wells were then incubated with increasing concentrations of biotinylated neurexin 1α* in binding buffer/Ca^{2+} (in triplicate) for 1 h. To develop the signal, wells were incubated with anti-streptavidin HRP conjugate (Sigma S2438; diluted 1:5000 in blocking buffer) for 45 min, washed three times with binding buffer/Ca^{2+} or binding buffer/EDTA, and then incubated with the substrate *o*-phenylenediamine (Calbiochem) for 10 min. The reaction was stopped by adding 50 μl/well 0.5 M H_2SO_4, and the absorbance was read at 490 nm. Data were analyzed with Prism (GraphPad). Specific binding was expressed as total binding in the presence of Ca^{2+} minus bind-

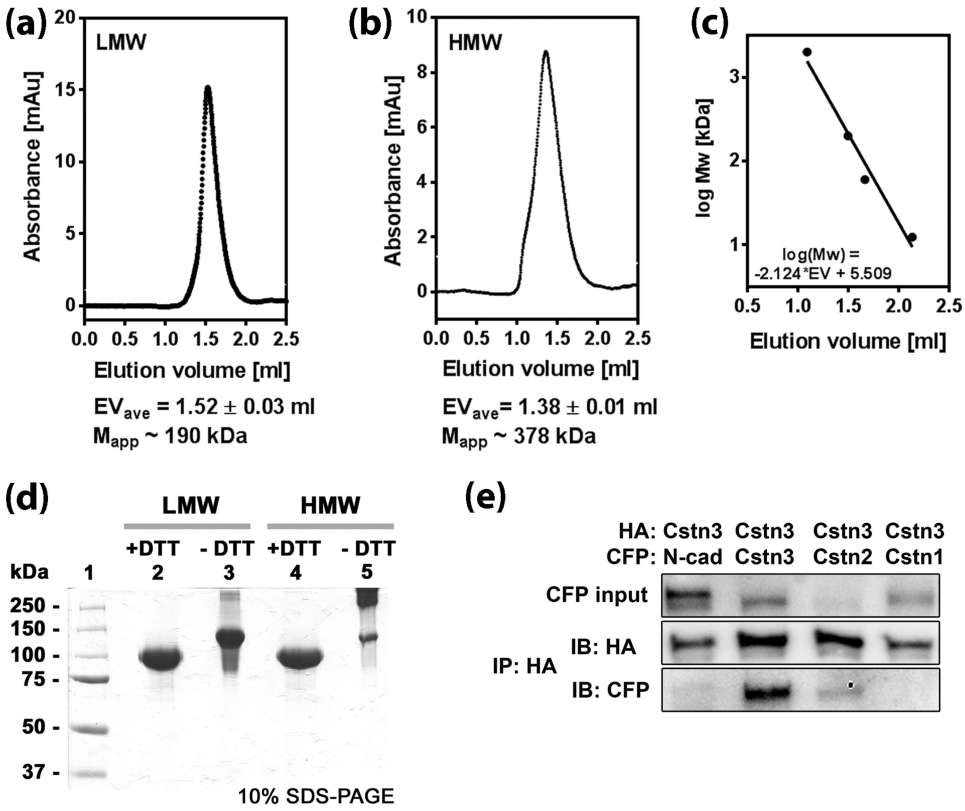

FIGURE 1. **Multimerization state of Cstn3.** Shown is size exclusion chromatography of Cstn3-LMW (*a*), Cstn3-HMW (*b*), and standards (2000, 200, 66, 29, and 12.4 kDa) (*c*). Each sample was run five times, and the average elution volume (EV_{ave}) is shown. Standards were run twice and deviated <0.02 ml between runs. Apparent molecular weights (M_{app}) reflect only the presence of "large" *versus* "small" species. *d*, SDS-PAGE analysis of Cstn3-LMW (10 μg; *lanes 2* and *3*) and Cstn3-HMW (10 μg; *lanes 4* and *5*) under reducing (+*DTT*) and non-reducing (−*DTT*) conditions. Markers are shown in *lane 1*. *e*, Cstn3 forms multimers in cell-based assays. HEK cells were co-transfected with HA-Cstn3 as well as N-cadherin-CFP, Cstn3-CFP, Cstn2-CFP, or Cstn1-CFP. Cell lysates were immunoprecipitated with anti-HA antibody and analyzed by Western blot (*IB*) compared with input (10% of immunoprecipitate (*IP*)). The relative signal intensity of co-immunoprecipitated proteins, normalized to precipitated HA-Cstn3 and input CFP signals, was 0.036 ± 0.016 for N-cadherin-CFP and 0.090 ± 0.044 for Cstn1-CFP relative to 1 for Cstn3-CFP (analysis of variance, $p < 0.0001$, and $p < 0.001$ comparing Cstn3 with Cstn1 or with N-cadherin in Bonferroni post hoc test, $n = 4$). The expression and co-immunoprecipitation data for Cstn2-CFP were highly variable.

ing in the absence of immobilized bait. The K_D was calculated by non-linear regression using a model for "one-site specific binding" and further visualized with Scatchard plots. *Error bars* show the S.E.

Surface Plasmon Resonance

Binding of neurexins to Cstn3 and NL2 was assessed in running buffer (10 mM HEPES, pH 7.4, 150 mM NaCl, 5 mM $CaCl_2$, and 0.05% Tween 20) at 25 °C on a Biacore T100. Cstn3 (860 RU) and NL2 (970 RU) were immobilized separately on C1 sensor chips (GE Healthcare). Specific binding data were obtained by injecting a series of neurexin concentrations over a ligand-coupled sensor and subtracting from the signal that collected simultaneously by flowing neurexins over a sensor with no ligand immobilized. The following neurexin concentrations were used: L1L6 and L1L5 (0, 4.7, 9.4, 18.8, 37.5, 75, and 150 nM); L5L6 (0, 4.7, 9.4, 18.8, 37.5, 75, 150, and 300 nM); n1β (0, 2.5, 5.0, 7.5, 10.0, 12.5, 15.0, 17.5, and 20 nM); and L2 (0, 4.7, 9.4, 18.8, 37.8, 75, 150, and 300 nM) flowed at 30 μl/min for 240 s (association step) followed by running buffer for 240 s (dissociation step). The sensor was regenerated after each protein injection with 5 M NaCl (for Cstn3/neurexin) or 10 mM HEPES, pH 7.4, 1 M NaCl, 3 mM EDTA, and 1% BSA (for NL2/neurexin). The data were processed using a kinetic analysis, and the K_D was calculated from sensorgram data fit to a 1:1 stoichiometric model. The K_D values for Cstn3-neurexin binding for two independent experiments were averaged (the average and S.D. are given). For NL2-neurexin binding, the standard errors on k_d and k_a calculated by the Biacore T100 software were used to calculate the error on the K_D. The molecular masses are as follows: n1α L1L6 (137,745 Da), n1α L1L5 (114,026 Da), n1α L5L6 (44,957 Da), n1α L5L6 SS#4 (48,521 Da), n1α L2 (20,147 Da), n1β (24,290 Da), Cstn3 (88,529 Da), and NL2 (64,784 Da).

Co-immunoprecipitation and Cell Surface Binding Assays

HEK cells were transfected with the indicated expression vectors (3) using TransIT-LT1 transfection reagent (Mirus) and grown for 48 h. Cell lysates were extracted with 1% Triton X-100 in TBS with Complete protease inhibitor (Roche Applied Science), incubated with 1 μg of anti-HA antibody (Roche Applied Science) overnight at 4 °C and then with Protein G beads for 1 h 4 °C. The beads were then washed with 0.1% Triton X-100 three times and eluted with SDS-sample buffer. Samples were analyzed by Western blot with anti-GFP antibody (Invitrogen). For the cell-based binding assay, COS7 cells were transfected with the indicated expression vectors (37) using TransIT-LT1 transfection reagent (Mirus) and grown for 24 h. Cstn3-Fc protein was generated as described previously (3).

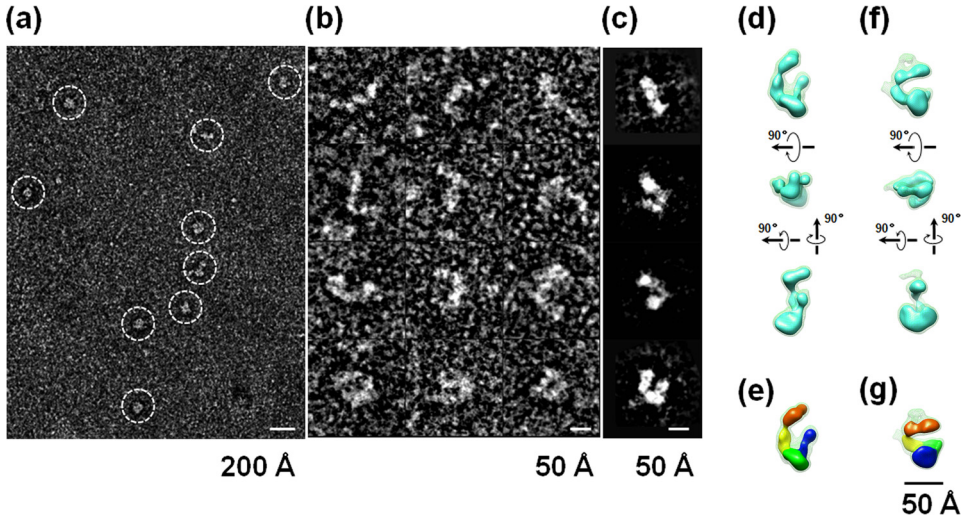

FIGURE 2. **Cstn3-LMW negative-stain EM images and three-dimensional reconstructions.** *a*, survey view of Cstn3 monomers (*dashed circles*). *b*, 12 representative raw images of Cstn3 monomers. *c*, four representative reference-free class averages. *d*, single-particle three-dimensional reconstruction using the first of two *ab initio* density maps obtained from IPET as an initial model (monomer reconstruction 1). Three orthogonal views are displayed using two isosurface contour levels (corresponding to volumes of ~50 and 25 kDa). *e*, high contour isosurface shown as in *d* was *colored* according to the molecular volumes of the four domains comprising the Cstn3 extracellular region (two cadherin domains in *orange* and *yellow*, LNS domain in *green*, and the α/β domain in *blue*). *f*, single-particle three-dimensional reconstruction using the second of two *ab initio* density maps obtained from IPET as an initial model (monomer reconstruction 2). Three orthogonal views are displayed using the same isosurface contour levels as above. *g*, same high contour isosurface shown as in *f* was *colored-coded* as in *e*. *Scale bars*, 200 Å (*a*) and 50 Å (*b–g*). The density maps have an effective resolution of ~16 Å based on the FSC = 0.5 criteria; see supplemental Fig. S1.

Live cells were incubated with 50 nM fusion proteins for 45 min at 4 °C. Fc fusions were visualized with FITC-conjugated anti-human IgG antibody.

RESULTS

Cstn3 Monomers and Tetramers—To study the structure of Cstn3, we expressed the Cstn3 ectodomain in insect cells and found that it formed two distinct molecular species, a low molecular weight (LMW) and a high molecule weight (HMW) multimeric form (Fig. 1, *a–c*). Under reducing conditions, both Cstn3-LMW and Cstn3-HMW migrated as ~100 kDa bands by SDS-PAGE, consistent with a monomer (Fig. 1*d*). However, under non-reducing conditions, Cstn3-HMW migrated as multimers held together with intersubunit disulfide bonds unlike Cstn3-LMW, which was clearly still monomeric (Fig. 1*d*). To test whether Cstn3 multimerizes with itself or other calsyntenin family members in a cellular environment, we co-expressed HA-tagged Cstn3 with CFP-tagged Cstn1, Cstn2, Cstn3, or the unrelated N-cadherin. We then pulled down HA-Cstn3 and probed if a CFP-tagged partner co-immunoprecipitated. HA-Cstn3 co-immunoprecipitated Cstn3-CFP, suggesting that Cstn3 forms multimers with itself, a specific association, as indicated by lack of co-precipitation of Cstn1-CFP or N-cadherin-CFP (Fig. 1*e*).

In EM micrographs, Cstn3-LMW corresponded to monomers that are flexible in structure (Fig. 2) and span a diameter of 85–100 Å (Fig. 3). Single-particle three-dimensional reconstruction was performed by multireference refinement methods (Fig. 2 and supplemental Fig. S1). Two separate single-particle reconstructions were carried out, each using a different *ab initio* density map obtained from IPET (34) as an initial model, and revealed conformational variability (monomer reconstruction 1 in Fig. 2, *d* and *e*, and monomer reconstruction 2 in Fig. 2, *f* and *g*). To relate the size of the individual domains to the

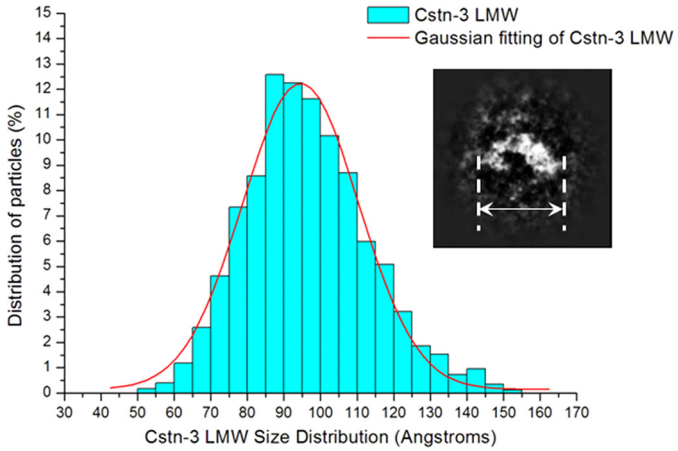

FIGURE 3. **Histogram of the Cstn3-LMW (monomer) diameters.** Cstn3 monomers were measured in their longest dimension (*double-headed arrow*). The histogram is displayed in *cyan bars*, and the distribution of the particle diameter is fitted by a *Gaussian curve*. The largest population (12.6%) has a diameter of 95.4 ± 2.5 Å.

complete Cstn3 ectodomain, homology models of the Cstn3 Cad1-Cad2 tandem and the LNS domain were docked in the molecular envelopes. The remaining density was assigned to the α/β domain, which lacks a clear structural homologue. Our reconstructions suggest that the Cstn3 monomer can adopt more opened or more closed conformations (Fig. 2, compare *e* and *g*).

In EM micrographs, Cstn3-HMW corresponded to multimers (Fig. 4 and supplemental Fig. S2). The multimers contained an internal 4-fold axis, suggestive of a tetramer, based on self-rotation and cross-correlation analysis of electron tomographic density maps from two independent particles (supplemental Fig. S2). The four monomers in the Cstn3 tetramer are related by a 90° rotation around a common 4-fold axis as

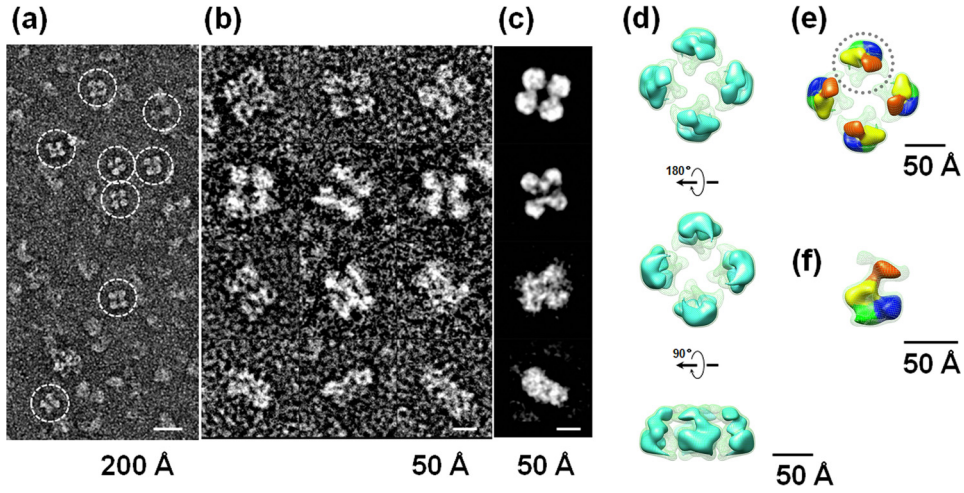

FIGURE 4. **Cstn3-HMW negative stain EM images and three-dimensional reconstruction.** *a*, survey view of Cstn3 tetramers (*dashed circles*). *b*, 12 representative raw images of Cstn3 tetramers. *c*, four representative reference-free class averages. *d*, single-particle three-dimensional reconstruction using an *ab initio* density map obtained from IPET as an initial model and refined with C_4 symmetry. Three orthogonal views are displayed using isosurface contour levels (corresponding to volumes of ~100 and 200 kDa). *e*, high contour isosurface shown as in *d* but *color-coded* according to domains as described in the legend for Fig. 2. *f*, extracted subunit *circled* in *e*. *Scale bars*, 200 Å (*a*) and 50 Å (*b–f*). The density maps have an effective resolution of ~16 Å based on the FSC = 0.5 criteria; see supplemental Fig. S2.

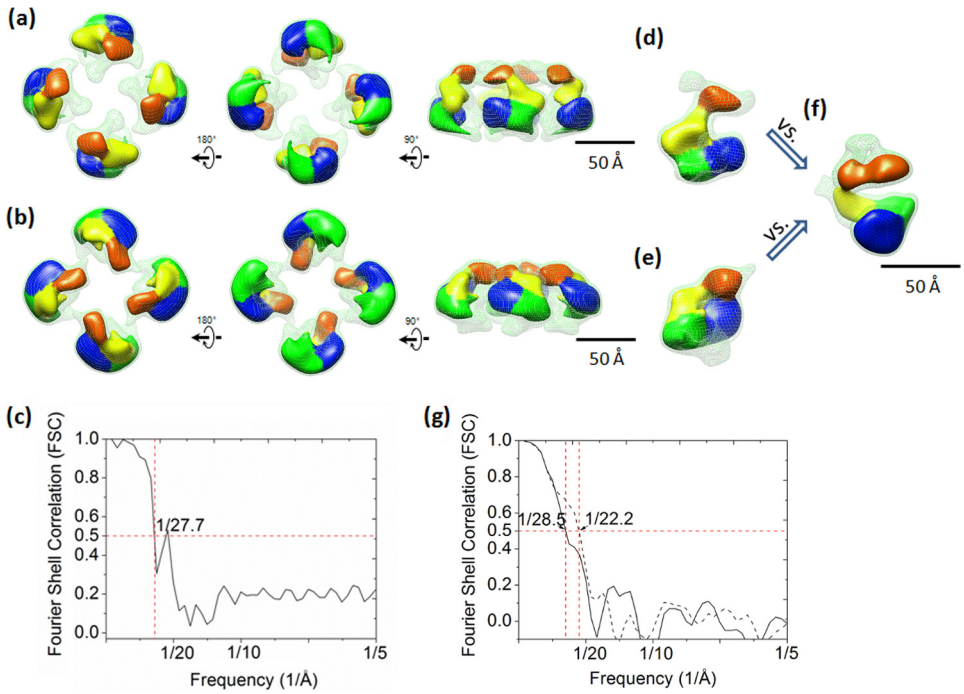

FIGURE 5. **Structural comparison of Cstn3 tetramers and their subunits with free Cstn3 monomers.** *a* and *b*, three orthogonal views of the two different Cstn3 tetramer three-dimensional single-particle reconstructions (tetramer reconstruction 1 and tetramer reconstruction 2), *colored* according to their domains (see the legend for Fig. 2). The density maps displayed as two isosurface contour levels were aligned with each other to facilitate structural comparison through FSC computation. *c*, the FSC curves of these two tetramers cross the 50% threshold at 28.0 Å. *d* and *e*, a monomer subunit extracted from each of the Cstn3 tetramer density maps. *f*, for comparison purposes, the Cstn3 monomer from Cstn3-LMW particles in the same view as *d* and *e*. *g*, FSC analyses on each subunit of the Cstn3 tetramers compared with the free Cstn3 monomer show that the FSC curves cross the 50% threshold at 22.2 and 28.5 Å, respectively.

opposed to a dimer of dimers. As in the case of the Cstn3 monomer, we performed single-particle three-dimensional reconstruction of the Cstn3 tetramer with refinement methods (31) using two different *ab initio* IPET reconstructions as initial models and applying C_4 symmetry (Fig. 4 and supplemental Fig. S2).

The Cstn3 tetramer resembles an unopened flower. Each monomer forms one of four petals. The N-terminal cadherin domains each form the tip of a petal, and the C-terminal portions form the base of the flower. The molecular symmetry of the Cstn3 tetramer is compatible with ectodomains tethered to the postsynaptic membrane by single C-terminal trans-membrane segments (5). Whereas the monomers flex somewhat in the tetramer (mimicking the slight opening of a flower), overall the conformation is similar between tetramer particles (Fig. 5), although only to a resolution of ~28 Å (*i.e.* significantly lower than the ~16 Å resolution of the monomer and tetramer reconstructions estimated with the FSC = 0.5 criteria) (supplemental Figs. S1*h* and S2*j*). The addition of Ca^{2+} significantly increased

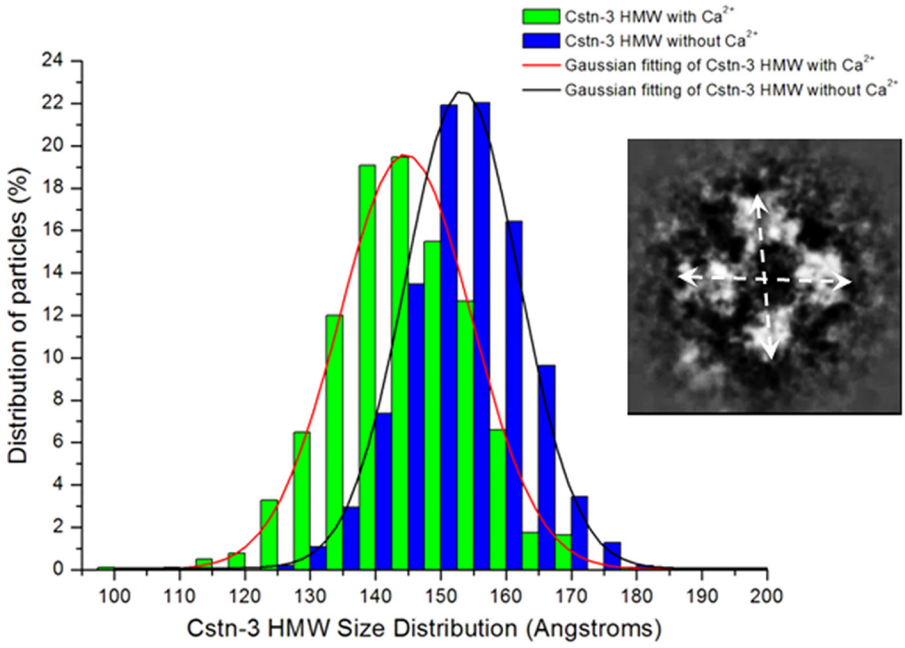

FIGURE 6. **Statistical analysis of Cstn3-HMW (tetramers) with and without Ca^{2+}.** Histograms of Cstn3 tetramer dimensions in buffer containing 3 mM $CaCl_2$ (*green bars*) compared with particles in buffer without additional $CaCl_2$ (*blue bars*). Distribution of the particle diameters fitted by a *Gaussian curve* show that the largest population of Cstn3 tetramers in the presence of Ca^{2+} has a diameter at 144.1 ± 2.5 Å (19.4%), whereas the largest population of Cstn3 tetramers without extra Ca^{2+} has a diameter of 152.5 ± 2.5 Å (22.0%).

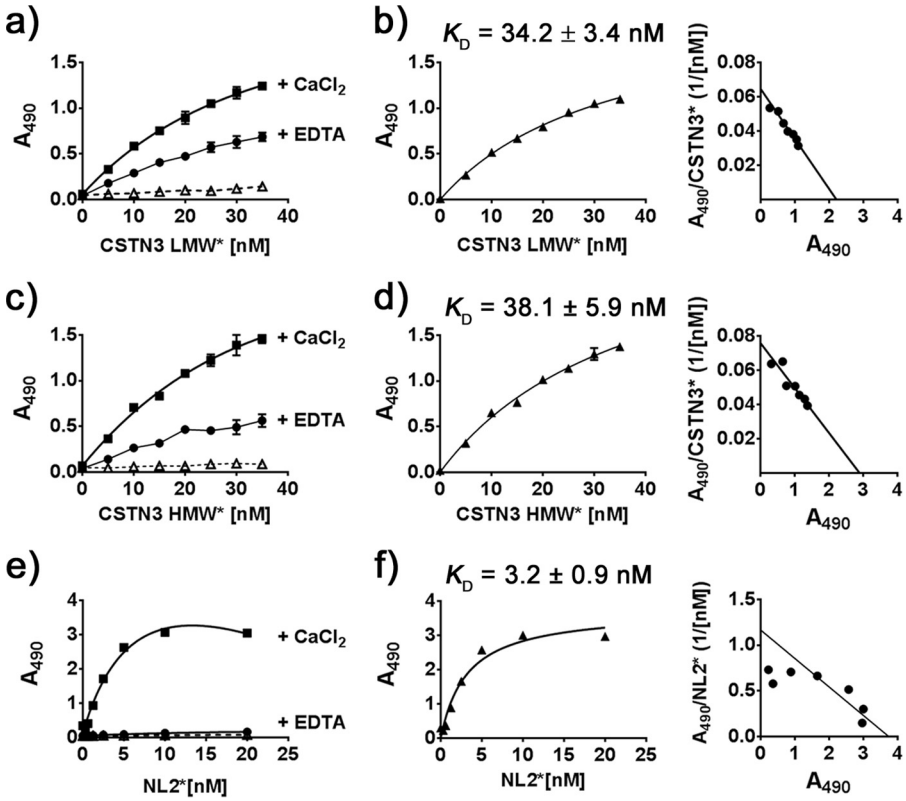

FIGURE 7. **Cstn3 binds immobilized n1α.** Increasing concentrations of biotinylated Cstn3-LMW* (monomer), Cstn3-HMW* (tetramer), and NL2* were incubated with immobilized n1α L1L6 in the presence of 5 mM $CaCl_2$ (■) or 20 mM EDTA (●). Wells lacking n1α (△) were also incubated with biotinylated proteins (see *a*, *c*, and *e*). Specific binding was expressed as total binding in presence of Ca^{2+} minus binding in absence of n1α and further visualized with Scatchard plots (see *b*, *d*, and *f*). *a*, binding Cstn3-LMW* and n1α; *b*, specific binding Cstn3-LMW* and n1α; *c*, binding Cstn3-HMW* and n1α; *d*, specific binding Cstn3-HMW* and n1α; *e*, binding NL2* and n1α; *f*, specific binding between NL2* and n1α. S.E. is shown. *Error bars*, S.E.

their compactness, reducing the diameter of the Cstn3 tetramers from ~150–160 Å (~30 μM $CaCl_2$) to ~135–145 Å (3 mM $CaCl_2$) (Fig. 6).

Cstn3 Binds Neurexin 1α—We used solid phase binding assays to test whether Cstn3 and n1α ectodomains bind directly. Cstn3 monomers bound immobilized n1α with high

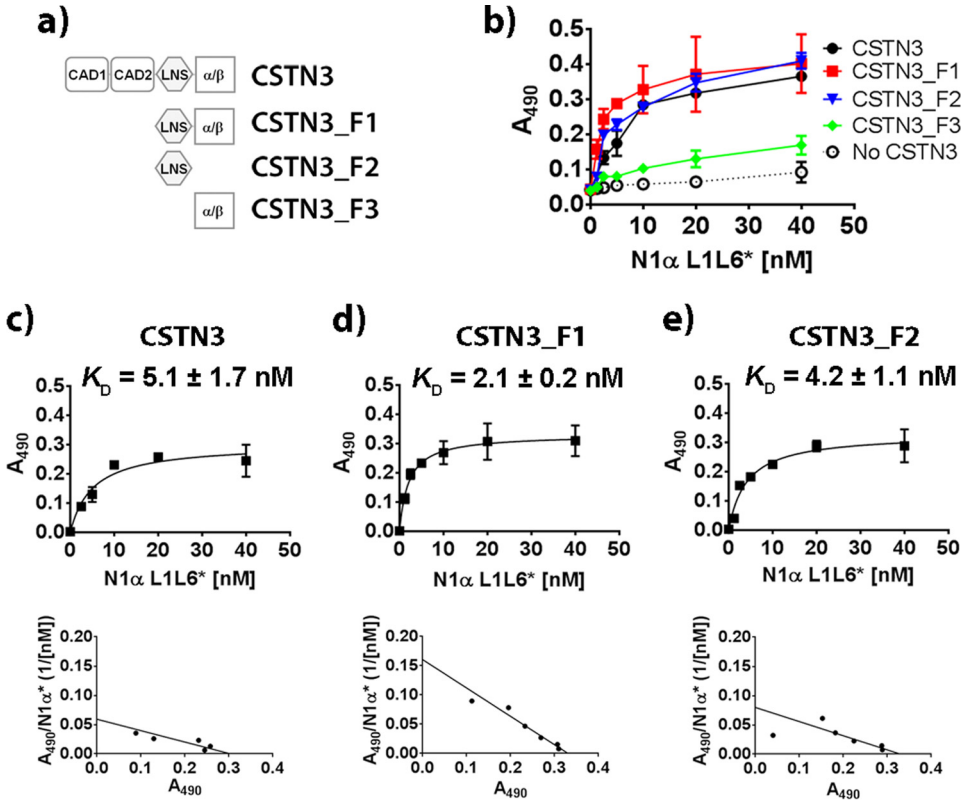

FIGURE 8. **n1α binds immobilized Cstn3.** Increasing concentrations of biotinylated n1α* were incubated with immobilized Cstn3 (and fragments). Wells lacking Cstn3 (*No Cstn3*) were also incubated with biotinylated proteins. Specific binding was expressed as total binding minus nonspecific binding and further visualized with Scatchard plots (see *c*, *d*, and *e*). *a*, domain structure of Cstn3 and fragments; *b*, total binding of Cstn3 and fragments to n1α*; *c*, specific binding of Cstn3 and n1α*; *d*, specific binding of Cstn3_F1 and n1α*; *e*, specific binding of Cstn3_F2 and n1α*. *Error bars*, S.E.

affinity (K_D = 34 ± 3 nM), and binding was promoted by Ca^{2+} (Fig. 7, *a* and *b*). Cstn3 tetramers interacted with n1α similarly (K_D = 38 ± 6 nM) (Fig. 7, *c* and *d*). For comparison, the ectodomain of the synaptic organizer NL2, another well validated Ca^{2+}-dependent binding partner, also bound n1α with high affinity (K_D = 3 ± 1 nM) (Fig. 7, *e* and *f*). To determine the minimal fragment of Cstn3 necessary to bind n1α, we tested the binding of n1α to immobilized Cstn3 and a series of Cstn3 fragments (Fig. 8, *a* and *b*). In this flipped assay, immobilized Cstn3 interacted with soluble n1α with even higher affinity (K_D = 5 ± 1 nM) (Fig. 8*c*). A Cstn3 fragment containing just the LNS and α/β domain bound n1α as well as full-length Cstn3, suggesting that the cadherin tandem is not required for high affinity binding (Fig. 8*d*). Indeed, the Cstn3 LNS domain alone was sufficient to bind n1α similarly to the full-length Cstn3 ectodomain (Fig. 8*e*), whereas the isolated α/β domain was not (Fig. 8*b*).

Cstn3 Uses a Distinct Mechanism to Interact with n1α—Because well known partners of n1α, such as neuroligins, LRRTMs, and latrophilin, strictly require the presence of the neurexin L6 domain for binding (15, 22, 38, 39), we tested this dependence for Cstn3 as well. Strikingly, the extracellular domain of n1α lacking EGF-C and L6 (L1L5) bound Cstn3 as well as the full-length n1α ectodomain containing all nine domains (Fig. 9, *a* and *b*). In contrast, interaction between NL2 and n1α was completely abolished when these two domains were absent (Fig. 9*c*). This suggests that Cstn3 and NL2 use different mechanisms to interact with n1α.

We confirmed the interaction between Cstn3 and n1α by surface plasmon resonance (Fig. 9, *d–f*). Full-length n1α (L1L6) bound Cstn3 similarly as the truncated ectodomain (L1L5) (*i.e.* K_D ~33 ± 8 nM and K_D ~45 ± 5 nM, respectively). The n1α fragment L5L6 also bound Cstn3 although more weakly (K_D ~105 ± 10 nM) (Fig. 9, *d* and *f*), whereas the presence of splice insert SS#4 did not significantly affect the interaction (L5L6 SS#4) K_D ~55 ± 10 nM (data not shown). In contrast, L1L6 and L5L6 bound NL2, but L1L5 (lacking the essential L6 domain) did not (Fig. 9, *e* and *f*). Furthermore, although L5L6 binds Cstn3 and NL2 with similar affinity (K_D ~105 ± 10 nM *versus* 83 ± 2 nM), different molecular mechanisms underlie these two interactions, because L5L6 associates with and dissociates from Cstn3 more slowly compared with its interaction with NL2, which quickly reaches equilibrium but also quickly falls apart (k_a ~17,370 ± 54 M^{-1} s^{-1} and k_d ~0.001823 ± 0.000006 s^{-1} for Cstn3 *versus* k_a ~67,030 ± 1000 M^{-1} s^{-1} and k_d ~0.00556 ± 0.000057 s^{-1} for NL2). The single neurexin L2 domain did not bind Cstn3 appreciably, indicating that very specific regions of the n1α ectodomain interact with Cstn3, whereas surprisingly, n1β also bound immobilized Cstn3, although the data did not fit a simple 1:1 stoichiometric model, clearly indicating a more complex binding mode and complicating quantitative assessment (data not shown). Thus, based on our solid phase binding and surface plasmon resonance assays, we conclude that the ectodomains of Cstn3 and n1α interact with each other directly.

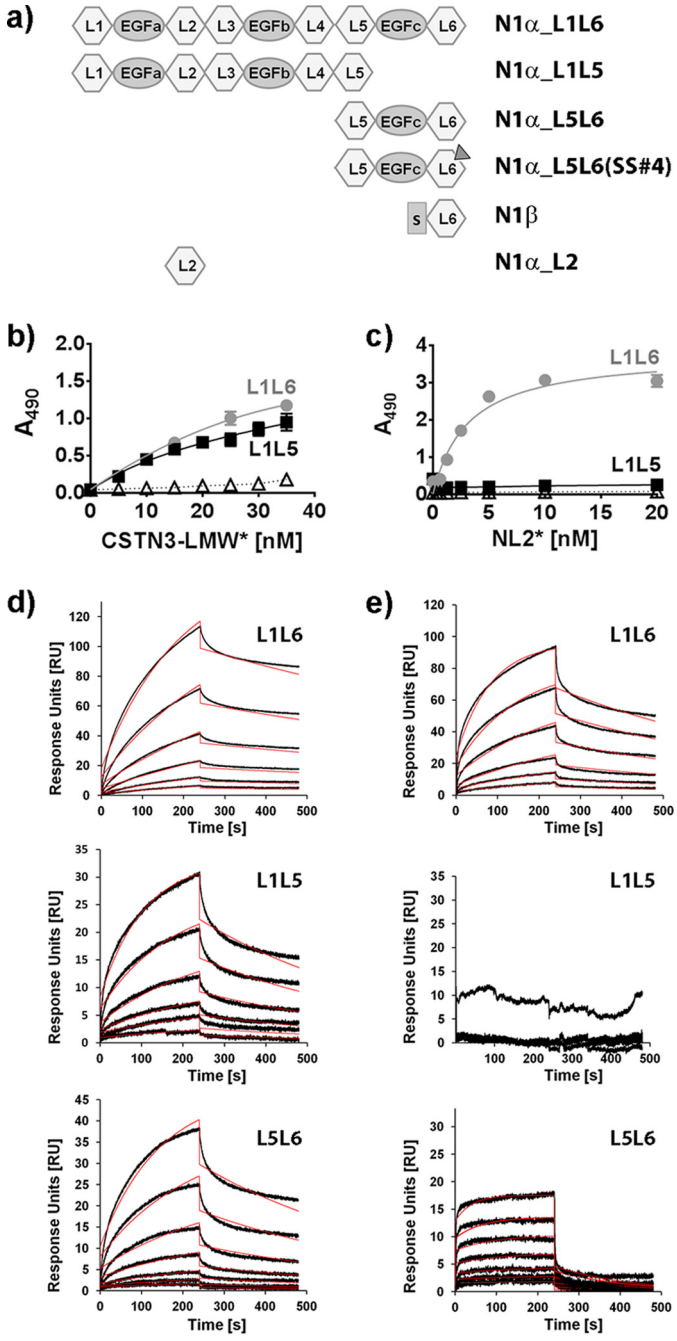

f)

	CSTN3 K_D [nM]	NL2 K_D [nM]
L1L6	32.5 ± 7.6	21.6 ± 0.4
L1L5	45.0 ± 4.6	-
L5L6	105.1 ± 10.4	82.9 ± 1.5

FIGURE 9. **Cstn3 binds n1α differently than NL2.** *a*, domain structure of n1α L1L6 and fragments used in this study. *b*, binding of biotinylated Cstn3* to immobilized n1α L1L6 (●), n1α L1L5 (■), or wells lacking n1α (△) in solid phase binding assays. *c*, binding of biotinylated NL2* to immobilized n1α L1L6 (●), n1α L1L5 (■), or wells lacking neurexin 1α (△) in solid phase binding assays; *d*, binding of soluble n1α and fragments to a Cstn3-coupled sensor by SPR. Binding curves of neurexin 1α L1L6 and L1L5 (4.7–150 nM), and L5L6 (4.7–300 nM) (in *black*) were fit to a 1:1 binding model (*red*). *e*, binding of soluble n1α and fragments to a NL2-coupled sensor by SPR as described in *d*; *f*, calculated K_D values.

We confirmed the domains mediating interaction between Cstn3 and n1α in cell-based binding assays (Fig. 10). Using a panel of n1α mutants lacking various domains expressed on the cell surface, we monitored the ability of these variants to bind soluble Cstn3-Fc. Consistent with the biochemical results, Cstn3-Fc bound cells expressing n1α L1L6, n1α L3L6, and n1α L5L6 similarly. Furthermore, the neurexin 1α mutation D1176A, which abolishes the Ca^{2+}-binding site in the L6 domain and prevents cell surface-expressed neurexin 1α from recruiting NL2 on the surface of dendrites in neuronal co-culture assays (37), had no effect on the interaction between Cstn3-Fc and n1α, substantiating that Cstn3 utilizes a different mechanism to bind neurexin 1α than NL2. In cell-based assays, we do not detect interaction between Cstn3 and n1β, although their soluble ectodomains interact in biochemical assays. Possibly, differences in glycosylation (by expressing proteins in COS cells, insect cells, and *Escherichia coli*) and/or the presentation of the proteins on the cell surface compared with our biochemical assays impacted binding.

DISCUSSION

We present here the first molecular insight into Cstn3. We used a unique combination of electron microscopy and tomography (34) to obtain unprecedented structural information on a multidomain and apparently flexible protein, intractable by other methods. The structures of Cstn3 were studied by optimized negative stain EM, a validated method that has proven successful for relatively small proteins (28), rather than conventional negative stain EM or cryo-EM. As with any negative stain EM technique, we cannot exclude potential artifacts as a result of its chemical characteristics, which might impact the resolution limit, the shape, and/or the conformation of the observed macromolecules. Therefore, structural interpretations must be made with due caution. Nevertheless, our reconstructions provide important biological insight in conjunction with our biochemical, biophysical, and cell-based assays. We show that the Cstn3 ectodomain forms monomers and tetramers that are stabilized by disulfide bonds and Ca^{2+} ions (Figs. 1, 2, 4, and 6) and that Cstn3 also forms multimers with itself in cell-based assays (Fig. 1*e*). The symmetry of the Cstn3 tetramer is compatible with four subunits tethered to a synaptic membrane. Importantly, the molecular 4-fold symmetry places putative protein binding sites similarly with respect to the synaptic membranes, facilitating the recruitment of partners from the presynaptic (trans-interaction) or the postsynaptic (cis-interaction) side.

The oligomerization state of synaptic organizers, such as Cstn3, is probably vital for their function. Neuroligins, for instance, dimerize prior to reaching the cell surface (40), and dimerization is required for their synaptogenic properties; indeed, artificial neuroligin monomers actively inhibit synaptic function (41, 42). On this basis, it has been proposed that neuroligin dimers induce presynaptic differentiation by mechanically clustering neurexins trans-synaptically (42, 43). Although

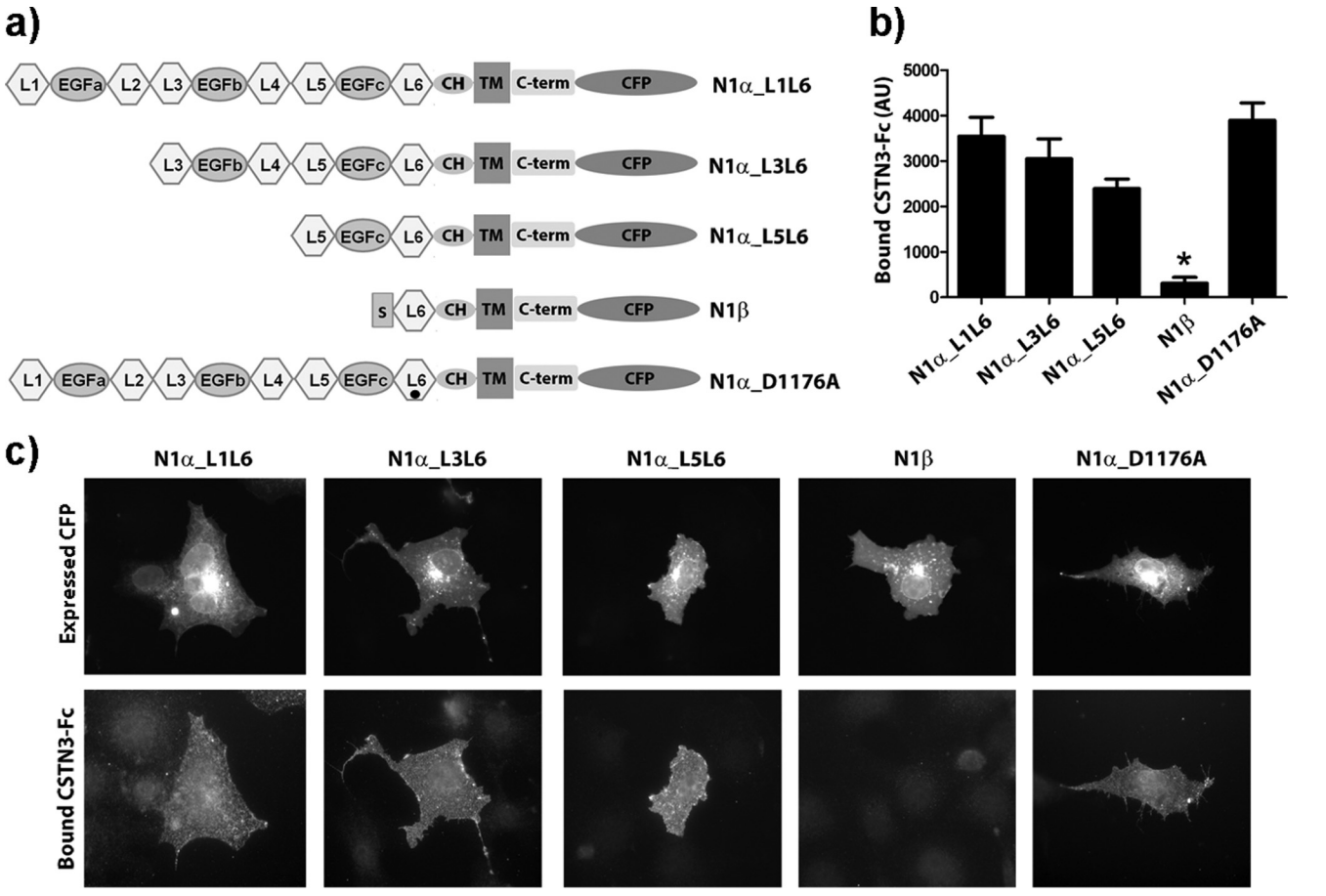

FIGURE 10. **Interaction of Cstn3 with neurexin 1α variants.** *a*, domain structure of the n1α L1L6 vector and mutants used in this study (*CH*, glycosylated region; *TM*, transmembrane domain; *C-term*, intracellular domain; *CFP*, C-terminal CFP tag). *b*, quantification of soluble Cstn3-Fc bound to COS cells expressing the indicated neurexin constructs on the cell surface (analysis of variance, $p < 0.0001$ ($n > 20$ cells each); *, $p < 0.001$ compared with n1α L1L6 by post hoc Bonferroni multiple comparison test). *c*, representative images of Cstn3-Fc bound to COS cells expressing n1α L1L6, n1α L3L6, n1α L5L6, and n1α D1176A but not n1β in cell-based binding assays. *Error bars*, S.E.

the ratio of Cstn3 monomers and tetramers in the brain is not known (nor whether it changes or yet other multimers exist), we show that Cstn3 monomers and tetramers bind n1α with similar affinity (Fig. 7; see below). According to the neuroligin-based model, Cstn3 tetramers would cluster neurexins, but Cstn3 monomers would not, raising the question of whether monomeric Cstn3 has a different or even opposing function in the synaptic cleft. Remarkably, more than 50% of Cstn3 is present in the brain as a soluble ectodomain shed through proteolysis (3). It will be important to determine whether Cstn3 monomers and tetramers are equally susceptible to ectodomain shedding. Strikingly, intersubunit disulfide bonds interconnect and stabilize the Cstn3 tetramer. Intersubunit disulfide bonds in the extracellular space are also known to stabilize the cis-dimer of E-cadherin, promoting homophilic adhesion (44), and cis-tetramers of γ-protocaderins (45). Calsyntenins play a role in cognition, and an increasing body of work suggests a link between oxidative status and neurodegenerative disorders (46), so it is tantalizing to speculate that oxidative stress in the brain might shift the balance between Cstn3 monomers and tetramers in the synaptic cleft by promoting intersubunit disulfide bond formation, thereby altering Cstn3 function. Further studies are needed to determine the multimerization state of Cstn3 in the synaptic cleft and the factors that regulate the balance between monomers and tetramers.

We show that the ectodomains of Cstn3 and n1α interact with each other directly with nanomolar affinity promoted by Ca^{2+} (Figs. 7–9). These data agree with cell-based assays, which observed similar Ca^{2+}-dependent interaction between a soluble Fc domain-fused Cstn3 ectodomain and cell surface expressed n1α (3) (Fig. 10). Interaction between Cstn3 and n1α involves the LNS domain of Cstn3 and L5-EGFC-L6 of n1α (Figs. 8–10). Whereas Cstn3 and NL2 both bind n1α with nanomolar affinity, promoted by Ca^{2+}, Cstn3 uses a different molecular mechanism to interact with n1α compared with NL2, one that does not rely on L6 (Figs. 9 and 10). Nevertheless, the Cstn3 binding site on n1α may be spatially close to L6 because the Cstn3 ectodomain can suppress the synapse-promoting activity of NL2 and LRRTM2 (3), possibly by competing for neurexin interaction. Presentation may also influence binding, because the soluble n1β ectodomain readily interacts with Cstn3 biochemically but in cell-based binding or recruitment assays does not (3) (Fig. 10). Likewise, the isolated Cstn3 LNS domain binds n1α in solid phase assays but when tethered to the cell surface does not, although this domain is certainly required for binding because its deletion or mutation disrupts

neurexin interaction and disrupts the synapse-promoting activity of Cstn3 (3). Although it is possible that technical aspects account for some of these minor differences, overall, the data presented here consistently and strongly indicate that Cstn3 interacts directly with n1α.

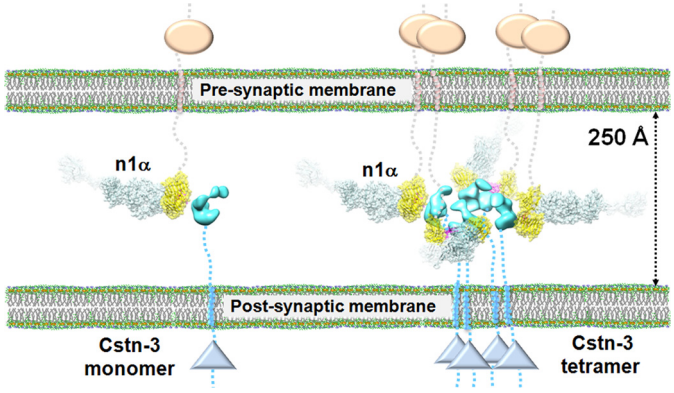

FIGURE 11. **Model of the interaction between Cstn3 and neurexin 1α at a synapse.** Monomeric Cstn3 would recruit a single neurexin 1α monomer (*left*), whereas Cstn3 tetramers would be able to recruit multiple neurexin 1α monomers (*right*), clustering the presynaptic and postsynaptic network more extensively. Neurexin 1α L2-L6 is shown (Protein Data Bank entry 3QCW) (16) with domains L1-EGF-A modeled in *translucently* to reflect their unknown location.

Our structural studies provide insight into the function of monomeric and tetrameric Cstn3 alone and in the context of a trans-synaptic bridge with n1α (Fig. 11). Although domains cannot be unambiguously assigned in our molecular envelopes of Cstn3, given their low resolution, our tentative assignment of the Cstn3 LNS domains places them in a ring on the outside of the Cstn3 tetramer where they could recruit potentially up to four n1α molecules. Other as yet unidentified partners could also bind Cstn3 to form mixed macromolecular assemblies. Interestingly, in the cerebellum, tetramers of the postsynaptic GluRδ2 receptor assemble four neurexins, which triggers synapse formation, although binding is indirect and requires a tripartite complex with cerebellins (47). The cadherin domains in Cstn3 appear to fulfill a role different from those seen in classical cadherins (48), because the N-terminal Cstn3 Cad1 domain does not mediate side-by-side dimers, and tryptophan residues underlying this interaction are not present (Fig. 12). Furthermore, the Cstn3 Cad1-Cad2 tandem aligns best with the internal EC2-EC3 in the five-domain mouse cadherin 8 (Fig. 12). However, similarly to cadherins, the interface between Cad1 and Cad2 in Cstn3 is probably rigidified by multiple Ca^{2+} ions binding between the adjacent domains because numerous calcium binding residues are conserved (Fig. 12).

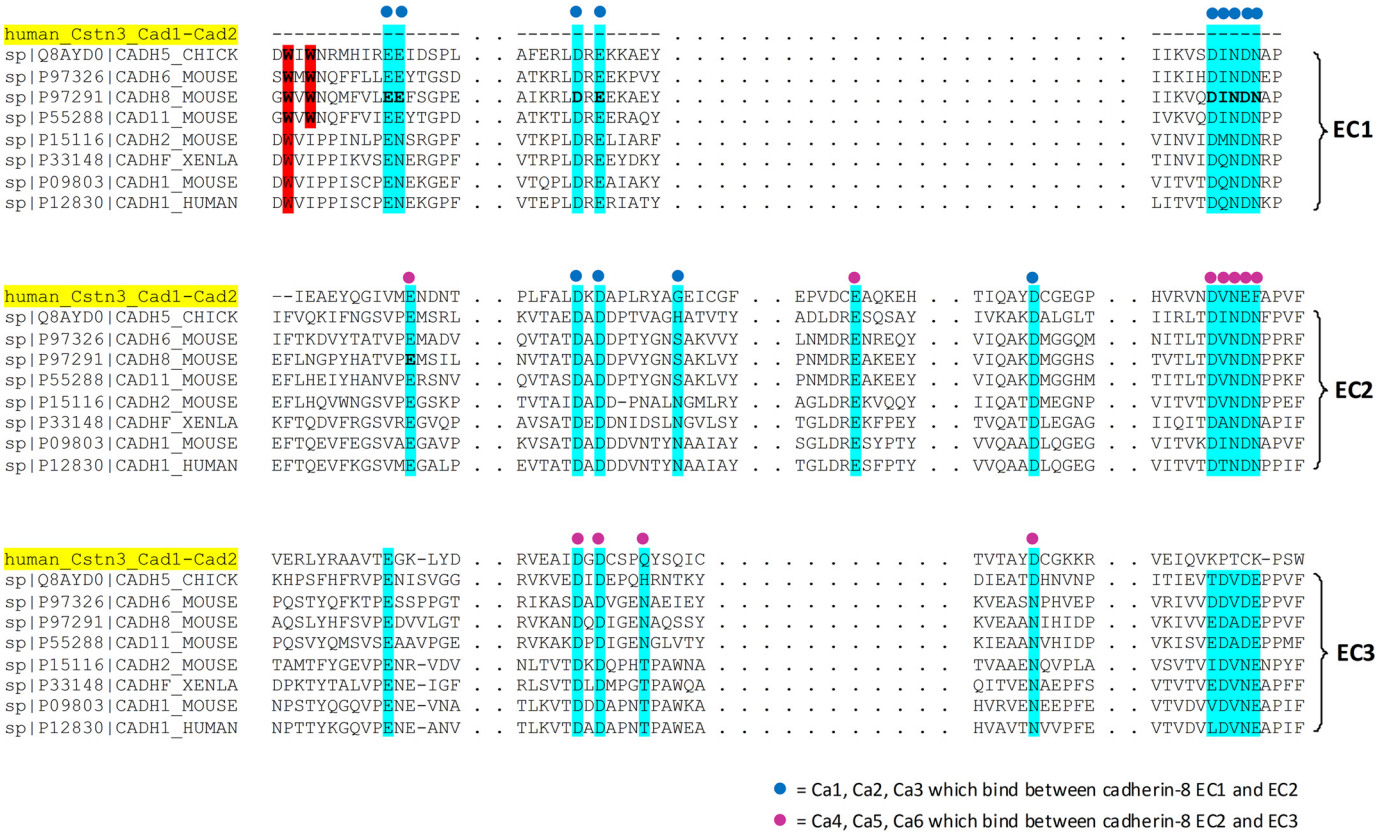

FIGURE 12. **Sequence comparison between Cstn3 Cad1-Cad2 and cadherin EC domains.** Shown is sequence alignment of human Cstn3 Cad1 and Cad2 with the EC1, EC2, and EC3 domains of chick cadherin 5 (Q8AYD0), mouse cadherin 6 (P97326), mouse cadherin 8 (P97291), mouse cadherin 11 (P55288), mouse cadherin 2 (P15116), frog cadherin (P33148), mouse cadherin 1 (P09803), and human cadherin 1 (P12830) using Clustal Omega. The human Cstn3 Cad1 and Cad2 domains align well with the EC2 and EC3 domains of cadherins. Cstn3 shares sequence identity with many of the residues that form Ca^{2+} binding sites in cadherin EC2, suggesting that the linker region between Cstn3 Cad1 and Cad2 is stabilized by Ca^{2+} ions as well. However, Cstn3 Cad2 lacks a characteristic critical stretch of five residues that forms part of the Ca^{2+}-binding sites that stabilize the linker region between cadherin EC3 and EC4. Tryptophan residues that underlie the strand swap dimerization mechanism of EC1 domains in cadherins are *boxed* in *red*. Amino acids aligning with the Ca^{2+}-binding residues found in mouse cadherin 8 EC1-EC2-EC3 are *highlighted* in *cyan*. *Blue* and *magenta spheres* indicate the identities of the Ca^{2+} ions bound in cadherins.

Our results support the idea that neurexins in combination with different interacting partners form very distinct heterophilic trans-synaptic bridges. We suggest that these trans-synaptic bridges are not intended to just align the intracellular presynaptic and postsynaptic machineries (that are attached to the respective cytoplasmic tails) but also to orient macromolecular assemblies in the synaptic cleft itself, altogether, recruiting and spatially organizing proteins into networks essential for synaptic function.

Acknowledgments—We thank Venugopal Vandavasi for preliminary studies, Dr. Naili Yue for carrying out statistical analysis of Cstn3 particles as a function of Ca^{2+}, and Dr. Thomas Südhof for the gift of the neuroligin 2 cDNA.

REFERENCES

1. Siddiqui, T. J., and Craig, A. M. (2011) Synaptic organizing complexes. *Curr. Opin. Neurobiol.* **21,** 132–143
2. Missler, M., Südhof, T. C., and Biederer, T. (2012) Synaptic cell adhesion. *Cold Spring Harb. Perspect. Biol.* **4,** a005694
3. Pettem, K. L., Yokomaku, D., Luo, L., Linhoff, M. W., Prasad, T., Connor, S. A., Siddiqui, T. J., Kawabe, H., Chen, F., Zhang, L., Rudenko, G., Wang, Y. T., Brose, N., and Craig, A. M. (2013) The specific α-neurexin interactor calsyntenin-3 promotes excitatory and inhibitory synapse development. *Neuron* **80,** 113–128
4. Um, J. W., Pramanik, G., Ko, J. S., Song, M. Y., Lee, D., Kim, H., Park, K. S., Südhof, T. C., Tabuchi, K., and Ko, J. (2014) Calsyntenins function as synaptogenic adhesion molecules in concert with neurexins. *Cell Rep.* **6,** 1096–1109
5. Hintsch, G., Zurlinden, A., Meskenaite, V., Steuble, M., Fink-Widmer, K., Kinter, J., and Sonderegger, P. (2002) The calsyntenins: a family of postsynaptic membrane proteins with distinct neuronal expression patterns. *Mol. Cell Neurosci.* **21,** 393–409
6. Papassotiropoulos, A., Stephan, D. A., Huentelman, M. J., Hoerndli, F. J., Craig, D. W., Pearson, J. V., Huynh, K. D., Brunner, F., Corneveaux, J., Osborne, D., Wollmer, M. A., Aerni, A., Coluccia, D., Hänggi, J., Mondadori, C. R., Buchmann, A., Reiman, E. M., Caselli, R. J., Henke, K., and de Quervain, D. J. (2006) Common Kibra alleles are associated with human memory performance. *Science* **314,** 475–478
7. Ikeda, D. D., Duan, Y., Matsuki, M., Kunitomo, H., Hutter, H., Hedgecock, E. M., and Iino, Y. (2008) CASY-1, an ortholog of calsyntenins/alcadeins, is essential for learning in *Caenorhabditis elegans*. *Proc. Natl. Acad. Sci. U.S.A.* **105,** 5260–5265
8. Hoerndli, F. J., Walser, M., Fröhli, Hoier, E., de Quervain, D., Papassotiropoulos, A., and Hajnal, A. (2009) A conserved function of *C. elegans* CASY-1 calsyntenin in associative learning. *PLoS One* **4,** e4880
9. Araki, Y., Tomita, S., Yamaguchi, H., Miyagi, N., Sumioka, A., Kirino, Y., and Suzuki, T. (2003) Novel cadherin-related membrane proteins, Alcadeins, enhance the X11-like protein-mediated stabilization of amyloid β-protein precursor metabolism. *J. Biol. Chem.* **278,** 49448–49458
10. Vagnoni, A., Perkinton, M. S., Gray, E. H., Francis, P. T., Noble, W., and Miller, C. C. (2012) Calsyntenin-1 mediates axonal transport of the amyloid precursor protein and regulates Aβ production. *Hum. Mol. Genet.* **21,** 2845–2854
11. Steuble, M., Diep, T. M., Schätzle, P., Ludwig, A., Tagaya, M., Kunz, B., and Sonderegger, P. (2012) Calsyntenin-1 shelters APP from proteolytic processing during anterograde axonal transport. *Biol. Open* **1,** 761–774
12. Francks, C., Maegawa, S., Laurén, J., Abrahams, B. S., Velayos-Baeza, A., Medland, S. E., Colella, S., Groszer, M., McAuley, E. Z., Caffrey, T. M., Timmusk, T., Pruunsild, P., Koppel, I., Lind, P. A., Matsumoto-Itaba, N., Nicod, J., Xiong, L., Joober, R., Enard, W., Krinsky, B., Nanba, E., Richardson, A. J., Riley, B. P., Martin, N. G., Strittmatter, S. M., Möller, H. J., Rujescu, D., St Clair, D., Muglia, P., Roos, J. L., Fisher, S. E., Wade-Martins, R., Rouleau, G. A., Stein, J. F., Karayiorgou, M., Geschwind, D. H., Ragoussis, J., Kendler, K. S., Airaksinen, M. S., Oshimura, M., DeLisi, L. E., and Monaco, A. P. (2007) LRRTM1 on chromosome 2p12 is a maternally suppressed gene that is associated paternally with handedness and schizophrenia. *Mol. Psychiatry* **12,** 1129–1139, 1057
13. Betancur, C., Sakurai, T., and Buxbaum, J. D. (2009) The emerging role of synaptic cell-adhesion pathways in the pathogenesis of autism spectrum disorders. *Trends Neurosci.* **32,** 402–412
14. Béna, F., Bruno, D. L., Eriksson, M., van Ravenswaaij-Arts, C., Stark, Z., Dijkhuizen, T., Gerkes, E., Gimelli, S., Ganesamoorthy, D., Thuresson, A. C., Labalme, A., Till, M., Bilan, F., Pasquier, L., Kitzis, A., Dubourgm, C., Rossi, M., Bottani, A., Gagnebin, M., Sanlaville, D., Gilbert-Dussardier, B., Guipponi, M., van Haeringen, A., Kriek, M., Ruivenkamp, C., Antonarakis, S. E., Anderlid, B. M., Slater, H. R., and Schoumans, J. (2013) NRXN1 and comprehensive review of the literature. *Am. J. Med. Genet. B Neuropsychiatr. Genet.* **162B,** 388–403
15. Südhof, T. C. (2008) Neuroligins and neurexins link synaptic function to cognitive disease. *Nature* **455,** 903–911
16. Chen, F., Venugopal, V., Murray, B., and Rudenko, G. (2011) The structure of neurexin 1α reveals features promoting a role as synaptic organizer. *Structure* **19,** 779–789
17. Miller, M. T., Mileni, M., Comoletti, D., Stevens, R. C., Harel, M., and Taylor, P. (2011) The crystal structure of the α-neurexin-1 extracellular region reveals a hinge point for mediating synaptic adhesion and function. *Structure* **19,** 767–778
18. Treutlein, B., Gokce, O., Quake, S. R., and Südhof, T. C. (2014) Cartography of neurexin alternative splicing mapped by single-molecule long-read mRNA sequencing. *Proc. Natl. Acad. Sci. U.S.A.* **111,** E1291–E1299
19. Rudenko, G., Nguyen, T., Chelliah, Y., Südhof, T. C., and Deisenhofer, J. (1999) The structure of the ligand-binding domain of neurexin Iβ: regulation of LNS domain function by alternative splicing. *Cell* **99,** 93–101
20. Sheckler, L. R., Henry, L., Sugita, S., Südhof, T. C., and Rudenko, G. (2006) Crystal structure of the second LNS/LG domain from neurexin 1α: Ca^{2+} binding and the effects of alternative splicing. *J. Biol. Chem.* **281,** 22896–22905
21. Graf, E. R., Kang, Y., Hauner, A. M., and Craig, A. M. (2006) Structure function and splice site analysis of the synaptogenic activity of the neurexin-1 β LNS domain. *J. Neurosci.* **26,** 4256–4265
22. Siddiqui, T. J., Pancaroglu, R., Kang, Y., Rooyakkers, A., and Craig, A. M. (2010) LRRTMs and neuroligins bind neurexins with a differential code to cooperate in glutamate synapse development. *J. Neurosci.* **30,** 7495–7506
23. Araç, D., Boucard, A. A., Ozkan, E., Strop, P., Newell, E., Südhof, T. C., and Brunger, A. T. (2007) Structures of neuroligin-1 and the neuroligin-1/neurexin-1 β complex reveal specific protein-protein and protein-Ca^{2+}-interactions. *Neuron* **56,** 992–1003
24. Fabrichny, I. P., Leone, P., Sulzenbacher, G., Comoletti, D., Miller, M. T., Taylor, P., Bourne, Y., and Marchot, P. (2007) Structural analysis of the synaptic protein neuroligin and its β-neurexin complex: determinants for folding and cell adhesion. *Neuron* **56,** 979–991
25. Chen, X., Liu, H., Shim, A. H., Focia, P. J., and He, X. (2008) Structural basis for synaptic adhesion mediated by neuroligin-neurexin interactions. *Nat. Struct. Mol. Biol.* **15,** 50–56
26. Shen, K. C., Kuczynska, D. A., Wu, I. J., Murray, B. H., Sheckler, L. R., and Rudenko, G. (2008) Regulation of neurexin 1beta tertiary structure and ligand binding through alternative splicing. *Structure* **16,** 422–431
27. Zhang, L., Song, J., Newhouse, Y., Zhang, S., Weisgraber, K. H., and Ren, G. (2010) An optimized negative-staining protocol of electron microscopy for apoE4.POPC lipoprotein. *J. Lipid Res.* **51,** 1228–1236
28. Rames, M., Yu, Y., and Ren, G. (2014) Optimized negative staining: a high-throughput protocol for examining small and asymmetric protein structure by electron microscopy. *J. Vis. Exp.* **90,** e51087
29. Grigorieff, N. (2007) FREALIGN: high-resolution refinement of single particle structures. *J. Struct. Biol.* **157,** 117–125
30. Frank, J., Radermacher, M., Penczek, P., Zhu, J., Li, Y., Ladjadj, M., and Leith, A. (1996) SPIDER and WEB: processing and visualization of images in 3D electron microscopy and related fields. *J. Struct. Biol.* **116,** 190–199
31. Ludtke, S. J., Baldwin, P. R., and Chiu, W. (1999) EMAN: semiautomated software for high-resolution single-particle reconstructions. *J. Struct. Biol.* **128,** 82–97

32. Kremer, J. R., Mastronarde, D. N., and McIntosh, J. R. (1996) Computer visualization of three-dimensional image data using IMOD. *J. Struct. Biol.* **116,** 71–76
33. Fernández, J. J., Li, S., and Crowther, R. A. (2006) CTF determination and correction in electron cryotomography. *Ultramicroscopy* **106,** 587–596
34. Zhang, L., and Ren, G. (2012) IPET and FETR: experimental approach for studying molecular structure dynamics by cryo-electron tomography of a single-molecule structure. *PLoS One* **7,** e30249
35. Pettersen, E. F., Goddard, T. D., Huang, C. C., Couch, G. S., Greenblatt, D. M., Meng, E. C., and Ferrin, T. E. (2004) UCSF Chimera: a visualization system for exploratory research and analysis. *J. Comput. Chem.* **25,** 1605–1612
36. Patel, S. D., Ciatto, C., Chen, C. P., Bahna, F., Rajebhosale, M., Arkus, N., Schieren, I., Jessell, T. M., Honig, B., Price, S. R., and Shapiro, L. (2006) Type II cadherin ectodomain structures: implications for classical cadherin specificity. *Cell* **124,** 1255–1268
37. Kang, Y., Zhang, X., Dobie, F., Wu, H., and Craig, A. M. (2008) Induction of GABAergic postsynaptic differentiation by α-neurexins. *J. Biol. Chem.* **283,** 2323–2334
38. Ko, J., Fuccillo, M. V., Malenka, R. C., and Südhof, T. C. (2009) LRRTM2 functions as a neurexin ligand in promoting excitatory synapse formation. *Neuron* **64,** 791–798
39. Boucard, A. A., Ko, J., and Südhof, T. C. (2012) High affinity neurexin binding to cell adhesion G-protein-coupled receptor CIRL1/latrophilin-1 produces an intercellular adhesion complex. *J. Biol. Chem.* **287,** 9399–9413
40. Poulopoulos, A., Soykan, T., Tuffy, L. P., Hammer, M., Varoqueaux, F., and Brose, N. (2012) Homodimerization and isoform-specific heterodimerization of neuroligins. *Biochem. J.* **446,** 321–330
41. Ko, J., Zhang, C., Arac, D., Boucard, A. A., Brunger, A. T., and Südhof, T. C. (2009) Neuroligin-1 performs neurexin-dependent and neurexin-independent functions in synapse validation. *EMBO J.* **28,** 3244–3255
42. Shipman, S. L., and Nicoll, R. A. (2012) Dimerization of postsynaptic neuroligin drives synaptic assembly via transsynaptic clustering of neurexin. *Proc. Natl. Acad. Sci. U.S.A.* **109,** 19432–19437
43. Dean, C., Scholl, F. G., Choih, J., DeMaria, S., Berger, J., Isacoff, E., and Scheiffele, P. (2003) Neurexin mediates the assembly of presynaptic terminals. *Nat. Neurosci.* **6,** 708–716
44. Makagiansar, I. T., Nguyen, P. D., Ikesue, A., Kuczera, K., Dentler, W., Urbauer, J. L., Galeva, N., Alterman, M., and Siahaan, T. J. (2002) Disulfide bond formation promotes the cis- and trans-dimerization of the E-cadherin-derived first repeat. *J. Biol. Chem.* **277,** 16002–16010
45. Schreiner, D., and Weiner, J. A. (2010) Combinatorial homophilic interaction between γ-protocadherin multimers greatly expands the molecular diversity of cell adhesion. *Proc. Natl. Acad. Sci. U.S.A.* **107,** 14893–14898
46. Grimm, S., Hoehn, A., Davies, K. J., and Grune, T. (2011) Protein oxidative modifications in the ageing brain: consequence for the onset of neurodegenerative disease. *Free Radic. Res.* **45,** 73–88
47. Lee, S. J., Uemura, T., Yoshida, T., and Mishina, M. (2012) GluRδ2 assembles four neurexins into trans-synaptic triad to trigger synapse formation. *J. Neurosci.* **32,** 4688–4701
48. Shapiro, L., and Weis, W. I. (2009) Structure and biochemistry of cadherins and catenins. *Cold Spring Harb. Perspect. Biol.* **1,** a003053

Protein Structure and Folding:

Calsyntenin-3 Molecular Architecture and Interaction with Neurexin 1 α

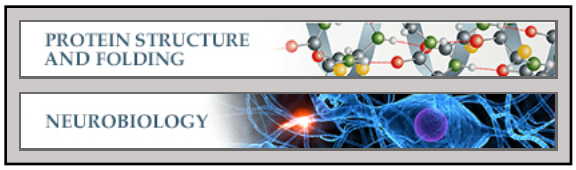

Zhuoyang Lu, Yun Wang, Fang Chen, Huimin Tong, M. V. V. V. Sekhar Reddy, Lin Luo, Suchithra Seshadrinathan, Lei Zhang, Luis Marcelo F. Holthauzen, Ann Marie Craig, Gang Ren and Gabby Rudenko

J. Biol. Chem. 2014, 289:34530-34542.
doi: 10.1074/jbc.M114.606806 originally published online October 28, 2014
